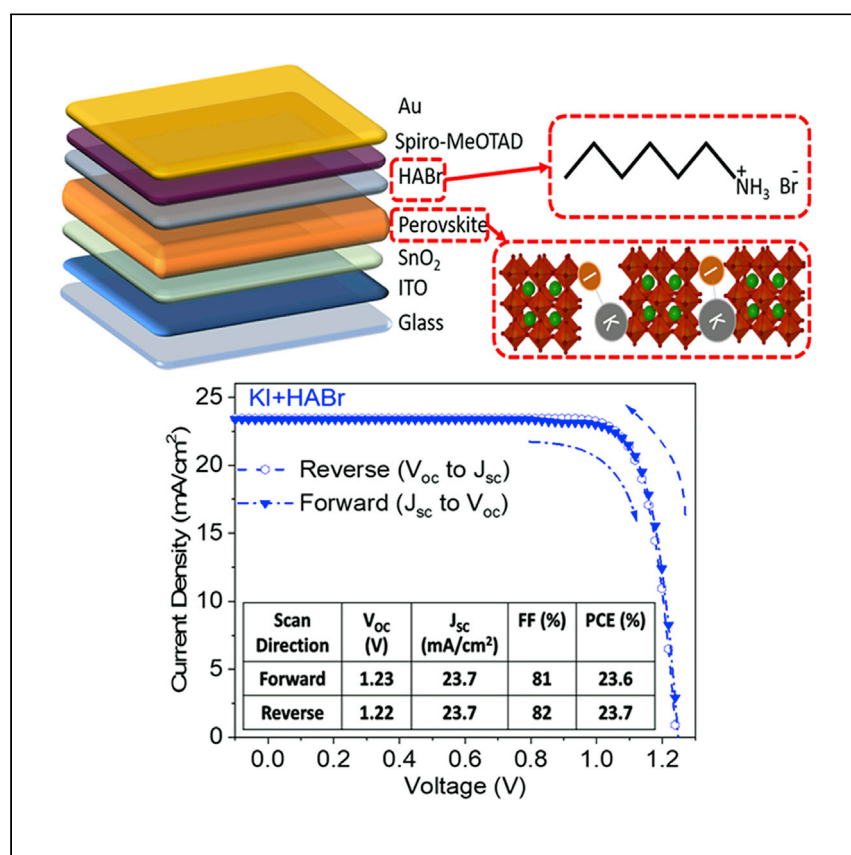


Article

Complementary bulk and surface passivations for highly efficient perovskite solar cells by gas quenching



Tang et al. report a 23.6% gas-quenched perovskite solar cell by incorporating potassium iodide (KI) in the precursor and applying n-hexylammonium bromide (HABr) to the surface. KI induces a spatial-compositional change, improving grain boundary properties. KI and HABr reduce traps close to the mid-gap, and HABr greatly improves the built-in potential of the device, thereby improving voltage output.

Shi Tang, Jueming Bing, Jianghui Zheng, ..., David R. McKenzie, Shujuan Huang, Anita W.Y. Ho-Baillie

anita.ho-baillie@sydney.edu.au

Highlights

Potassium iodide induces a compositional change, improving grain boundary properties

n-Hexylammonium bromide improves the built-in potential of the device

Close to mid-band-gap defects can be effectively passivated by complementary passivation



Article

Complementary bulk and surface passivations for highly efficient perovskite solar cells by gas quenching

Shi Tang,^{1,2,3,4} Jueming Bing,^{1,2,3} Jianghui Zheng,^{1,2,3} Jianbo Tang,⁵ Yong Li,³ Mohannad Mayyas,⁵ Yongyoon Cho,⁶ Timothy W. Jones,⁴ Terry Chien-Jen Yang,⁴ Lin Yuan,⁷ Mike Tebyetekerwa,⁸ Hieu T. Nguyen,⁸ Michael P. Nielsen,³ N.J. Ekins-Daukes,³ Kourosh Kalantar-Zadeh,⁵ Gregory J. Wilson,⁴ David R. McKenzie,¹ Shujuan Huang,^{3,7} and Anita W.Y. Ho-Baillie^{1,2,3,4,9,*}

SUMMARY

The power conversion efficiency (PCE) of metal halide perovskite solar cells (PSCs) has improved dramatically from 3.8% to 25.5% in only a decade. Gas quenching is a desirable method for fabricating high-efficiency cells as it does not consume antisolvents and is compatible with large-area deposition methods such as doctor blading and slot-die coating. To further improve PCEs for gas-quenched PSCs, here, we develop complementary bulk and surface passivation strategies by incorporating potassium iodide (KI) in the perovskite precursor and applying n-hexylammonium bromide (HABr) to the perovskite surface. We show that (1) KI induces a spatial-compositional change, improving grain boundary properties; (2) KI and HABr reduce traps, especially at levels close to the mid-gap; and (3) HABr greatly improves the built-in potential of the device, thereby improving voltage output. The champion device achieves a steady-state PCE of 23.6% with a V_{OC} of 1.23V, which is, to the best of our knowledge, the highest for PSC by gas quenching to date.

INTRODUCTION

Metal halide perovskites have attracted tremendous research interest due to their extraordinary optoelectronic properties^{1–7} that led to the rapid improvement in the power conversion efficiency (PCE) of perovskite solar cells (PSCs) from 3.8% to 25.5% in only a decade.⁸ Devices achieving >20% PCE can be demonstrated at ease using the antisolvent dripping method.^{9–11} However, the amount of antisolvent is 3–5 times the volume of the perovskite precursor, and some of the antisolvents used are toxic, which inevitably increases the manufacturing costs of PSCs.^{12–14} Antisolvent treatments are limited in their applications for scalable deposition methods such as doctor blading and slot-die coating. To circumvent this without compromising the performance of PSCs, the gas-quenching method has been demonstrated for the fabrication of high-efficiency cells when applied to spin coating,^{15–26} slot-die coating,^{27–29} doctor-blade coating,^{30–32} and roll-to-roll printing³³ for the deposition of perovskite thin films. However, there is still room for improvement for the PCEs of PSCs by gas quenching. Open circuit voltages (V_{OC} s) and short-circuit current densities (J_{SC} s) of gas-quenched devices are typically below 1.2 V and 23.5 mA/cm², respectively. The low J_{SC} is due to the larger-than-ideal band gaps of the perovskite absorbers⁵ used and non-optimized

¹School of Physics, The University of Sydney, Sydney, NSW 2006, Australia

²The University of Sydney Nano Institute, The University of Sydney, Sydney, NSW 2006, Australia

³Australian Centre for Advanced Photovoltaics (ACAP), School of Photovoltaic and Renewable Energy Engineering, University of New South Wales, Sydney, NSW 2052, Australia

⁴CSIRO Energy, Newcastle Energy Centre, 10 Murray Dwyer Circuit, Mayfield West, NSW 2304, Australia

⁵School of Chemical Engineering, University of New South Wales (UNSW) Sydney Campus, Sydney, NSW, Australia

⁶Department of Polymer Chemistry, Graduate School of Engineering, Kyoto University, Katsura, Nishikyo-ku, Kyoto 615-8510, Japan

⁷School of Engineering, Sustainable Energy Research Centre, Macquarie University, Sydney, NSW 2109, Australia

⁸Research School of Electrical, Energy, and Materials Engineering, College of Engineering and Computer Science, The Australian National University, Canberra, ACT 2601, Australia

⁹Lead contact

*Correspondence: anita.ho-baillie@sydney.edu.au
<https://doi.org/10.1016/j.xcrp.2021.100511>



optical management in these cells, as well as the presence of non-radiative recombination within the perovskite bulk (e.g., at the grain boundaries) and at perovskite surfaces, which also contributes to lower V_{OC} . Low V_{OC} is also due to poor band alignment at the perovskite-carrier transport layer interface.^{6,7} This suggests that developing surface and grain boundary passivations compatible with gas-quenched-processed perovskite films is critical.

Here, we report complementary bulk and surface passivation strategies using potassium iodide (KI)-incorporated perovskite precursor^{17,34,35} and n-hexylammonium bromide (HABr) surface treatment.³⁶ First, we show that KI narrows the band gap of perovskite absorbers, which extend the optical absorption and reduce non-radiative recombination in the perovskite thin films, thereby increasing the output voltage of perovskite solar cells.^{17,34} Second, HABr forms a very thin low-dimensional perovskite layer passivating the surface and grain boundaries of the perovskite thin film,³⁶ as evidenced by the results of conductive atomic force microscopy (c-AFM) and depth profile and angle-resolved X-ray photoelectron spectroscopy (XPS). The end result is improved built-in potential, and therefore improved current output of associated devices. Finally, the passivation strategies developed using KI and HABr are shown to greatly reduce traps at different energy levels. This work is the first to report the density and distribution of trap states in gas-quenched processed perovskites before and after various passivations. The champion gas-quenched PSC achieved a 23.6% steady-state PCE with a V_{OC} of 1.23 V, retaining 90% of its initial PCE after 30 days of N_2 storage. To the best of our knowledge, this is the highest PCE for PSCs fabricated by the gas-quenching method to date (Figure 1F). This is significant for low solvent (therefore, lower cost and reduced toxicity) and scalable manufacturing of efficient PSCs. The complementary passivations reported here are not only suitable for PSCs fabricated by the gas-quenching method but they are also readily translatable to other scalable processes for improved efficiency.

RESULTS AND DISCUSSION

Fabrication and characterization

Figure 1A illustrates the gas-quenching method that replaces the antisolvent dripping for the fabrication of $FA_{0.80}MA_{0.15}Cs_{0.05}Pb_{1.55}Br_{0.45}$ perovskite film. As shown, N_2 gas was blown to the substrate during the deposition of perovskite precursor solution by spinning to induce supersaturation.³⁷ Figure 1B shows the structure of PSCs demonstrated in this work, as well the complementary passivation strategies developed that involve the incorporation of KI into the perovskite precursor and HABr surface treatment to passivate the perovskite-spiro-OMeTAD interface (spiro-OMeTAD = 2,2',7,7'-tetrakis-9,9'-spirobifluorene, and is used as the hole transport layer for the PSC). Figure S1 shows the distribution of electrical characteristics of reference cells, KI passivated, and KI+HABr passivated cells. The PCE improvements after KI incorporation, especially when in conjunction with HABr treatment, are mainly due to increases in V_{OC} and fill factor (FF). The treatments also narrow the spread of J_{SC} for cells. The photocurrent density-voltage (J-V) curves of the best PSC under reverse and forward scans are shown in Figure 1C, demonstrating negligible hysteresis. Reverse scanned, forward scanned, and PCEs exceed 23% (Figures 1C and 1D). The external quantum efficiency of the champion cell is consistently high at 90% below the optical threshold and the integrated J_{SC} is 23.6 mA/cm², which agrees well with that measured from light J-V measurement.

Role of KI incorporation and HABr surface treatment

To understand how KI incorporation and HABr surface treatment improve device performance, X-ray diffraction (XRD), photoluminescence (PL), and time-resolved

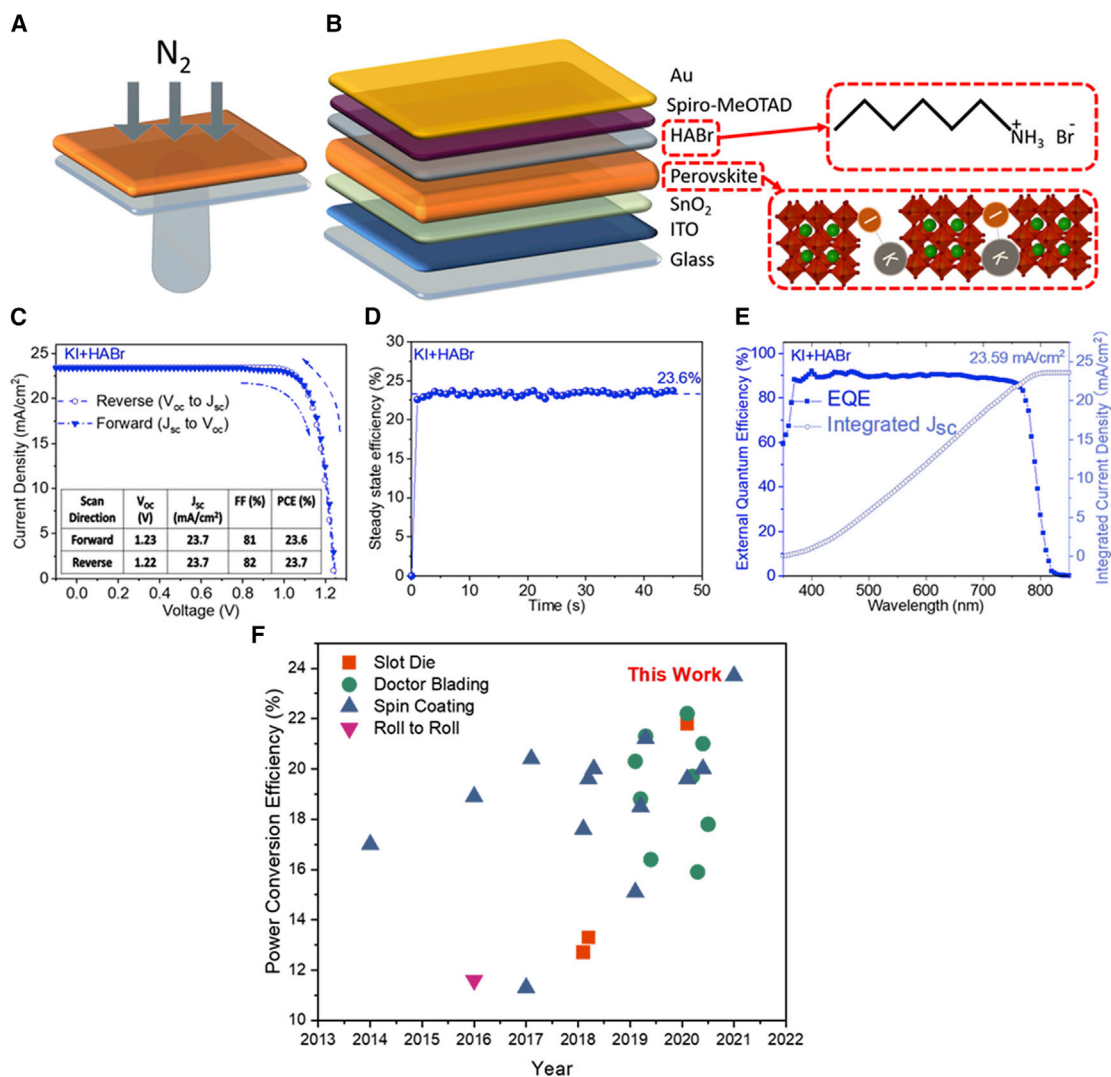


Figure 1. Complementary passivations for highly efficient perovskite solar cells by gas quenching

(A) Gas quenching method for fabricating perovskite thin films.

(B) Device structure of PSCs demonstrated using complementary passivations scheme developed in this work. KI was incorporated into the perovskite precursor, while HABr was deposited on the surface of the perovskite film.

(C) Current density-voltage curve of gas-quenched with KI+HABr passivated PSCs.

(D) Steady-state PCE of gas-quenched with KI+HABr passivated PSCs.

(E) External quantum efficiency of gas-quenched with KI+HABr passivated PSCs.

(F) Evolution of PCE of perovskite solar cells by gas quenching over time showing highest value achieved to date by this work. Details can be found in Table S1.

photoluminescence (TRPL) were carried out on test structures. Figures 2A and 2B show the XRD patterns of reference, KI, and HABr passivated perovskite thin films. The undesirable photoinactive δ -phase of FAPbI₃ and residual PbI₂ is present in the reference samples, which are effectively removed after KI incorporation.³⁸

The most significant impact of KI incorporation is seen in the PL spectra shown in Figure 2C. KI incorporation causes a peak redshift from 788 to 794 nm and an increase in PL intensity. This redshift suggests a compositional change in the perovskite thin film, possibly due to I⁻/Br⁻ exchange in the perovskite film, making it more iodide rich^{17,34} or the formamidinium (FA) redistribution making the film FA poor.³⁹ This hypothesis

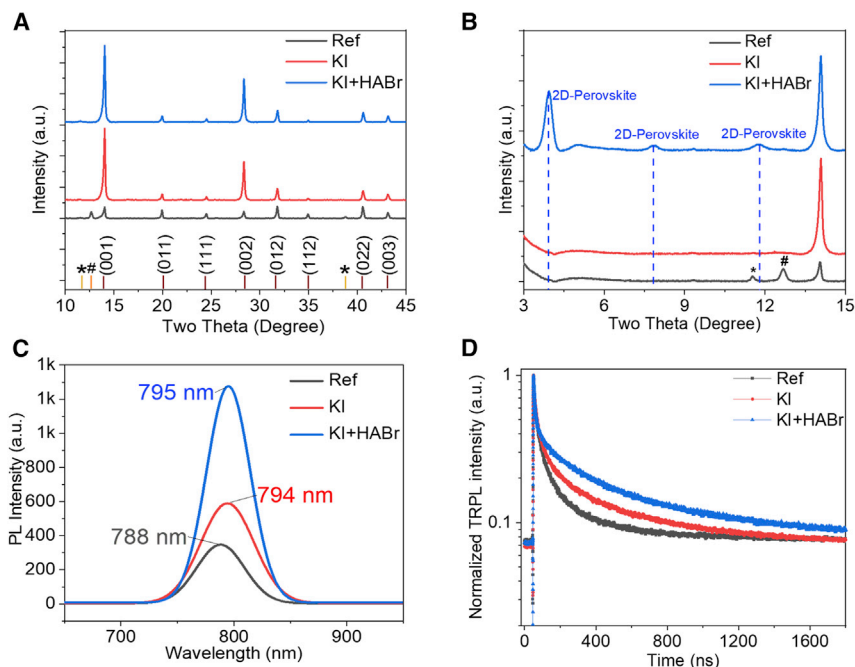


Figure 2. Material properties of KI and HABr passivated perovskite films by gas quenching

(A and B) XRD pattern (*, #, and 2D-perovskite represents the δ -phase of FAPbI₃, PbI₂, and 2-dimensional perovskite, respectively).

(C) PL spectra of reference, KI passivated, and KI+HABr passivated samples.

(D) TRPL spectra of reference, KI passivated, and KI+HABr passivated samples.

will be tested by AFM-infrared spectroscopy (AFM-IR), which is presented below. In terms of the additional HABr treatment, the impact on the PL peak shift is insignificant (from 794 to 795 nm). In terms of the XRD pattern of the KI+HABr passivated sample, the presence of 3.93°, 7.86°, and 11.79° peaks (Figure 2B) suggests the formation of 2-dimensional (2D) perovskite, and these peaks are in good agreement with the previous report of Yoo et al.³⁶ The effect can also be seen in the plan-view scanning electron microscopy (SEM) image in Figure S2C.

The trends in the rise of PL intensities from the KI and KI+HABr samples are similar to those for the rise of effective TRPL lifetimes (τ_{eff}) (Table S2) in the same samples as shown in Figure 2D. Details for TRPL fitting and the determination of τ_{eff} can be found in the Experimental procedures. τ_{eff} increases from 66 to 108 ns after KI incorporation and increases further to 129 ns after HABr surface treatment. PL quantum yield (Figure S3) and quasi-Fermi-level splitting⁴⁰ (Table S3) for the test structures before and after KI and KI+HABr treatments were also determined showing the same trends pointing to the effectiveness of KI and HABr in improving film quality. Reasons are discussed below using spatially resolved analysis.

Topography and current mappings by c-AFM on reference, KI passivated, and KI+HABr passivated perovskite films are shown in Figures 3A–3F, respectively. For the reference perovskite thin film, grain boundaries are more conductive than the grain interior as shown by c-AFM images (Figure 3D). However, the incorporation KI causes the grain boundaries to become less conductive, reducing the differences between grain interior and grain boundaries (Figure 3E). The elimination of PbI₂ from the grain boundaries (although evident in Figures 2A and S2B) is unlikely to be the cause of reduced

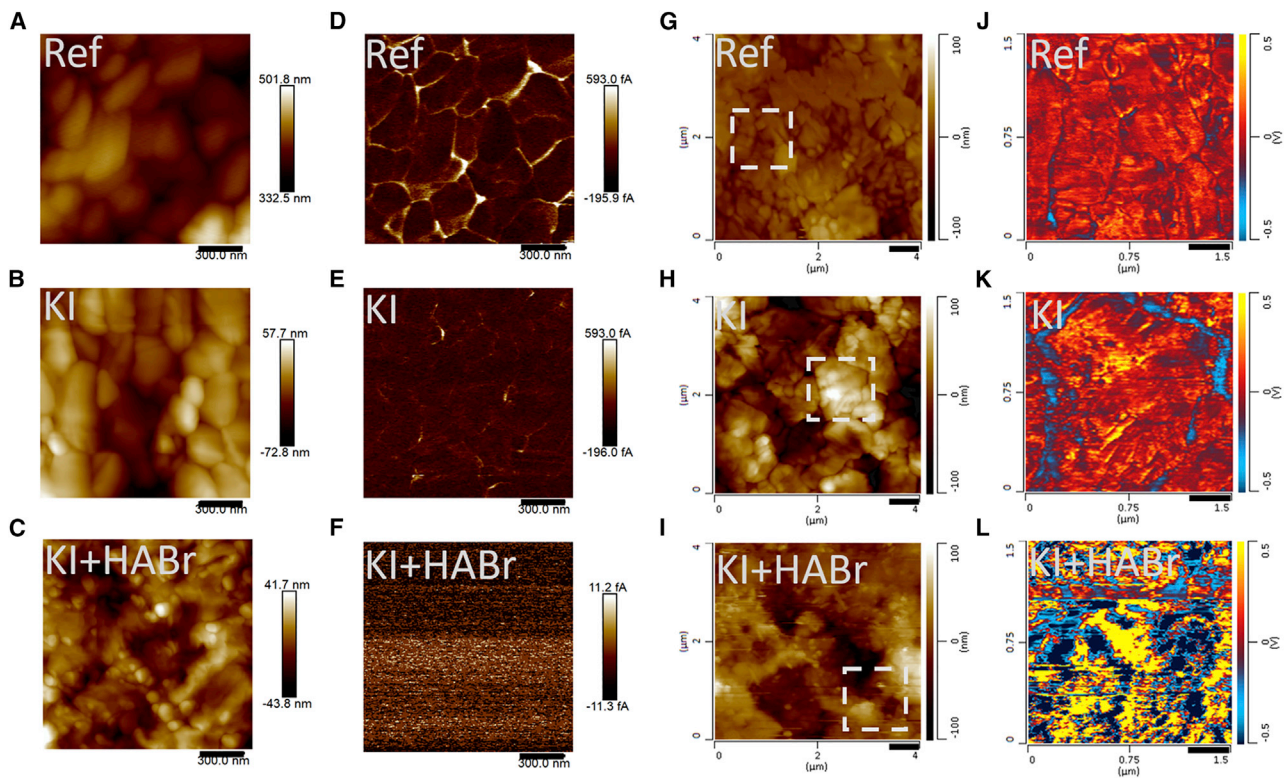


Figure 3. Spatially resolved analyses of Ref, KI, and HABr passivated perovskite films by gas quenching
(A–C) Topography map of (A) reference, (B) KI passivated, and (C) KI+HABr passivated perovskite films.
(D–F) Current mapping by c-AFM of the same samples.
(G–L) AFM-IR mapping of the 1,715 cm^{-1} wavenumber for a given region of the same samples.
Scale bars are 300 nm.

conductivity due to the lower mobility of PbI_2 compared with the perovskite.⁴¹ Rather, it is likely to be due to the reduction in positively charged iodide vacancies (V_{I^+}), which are dominant defects at grain boundaries, and when present, have been reported to enhance the conductivity of the grain boundaries due to ionic contributions dominating in the dark.^{42,43}

HABr surface treatment on KI samples reduces the conductivity of the perovskite thin film, further resulting in the measured signal being close to the detection limit (Figure 3F). This is due to the formation of a thin and less conductive 2D perovskite layer on the surface. It is important to note that both KI and HABr do not affect the series resistance of the final perovskite devices. This is because the conductivity measured by c-AFM includes the lateral conductivity of the film, which does not affect the operation of the final solar device as it is designed in such a way that only vertical carrier transport matters the most and lateral current flow is handled efficiently by the transparent conductive oxide and metal electrode in the final solar device. The reduced lateral conductivity is likely to produce an additional benefit of localizing defect-related and shunting-related effects, thereby increasing the FF and shunt resistance in KI-incorporated and HABr-treated cells (Figure S1).

For further chemical analysis of various films, we carried out AFM-IR, depth-profile XPS, and angle-resolved XPS. Figures 3G–3I show the AFM topography of the reference, KI passivated, and KI+HABr passivated samples, and Figures 3J–3L show the

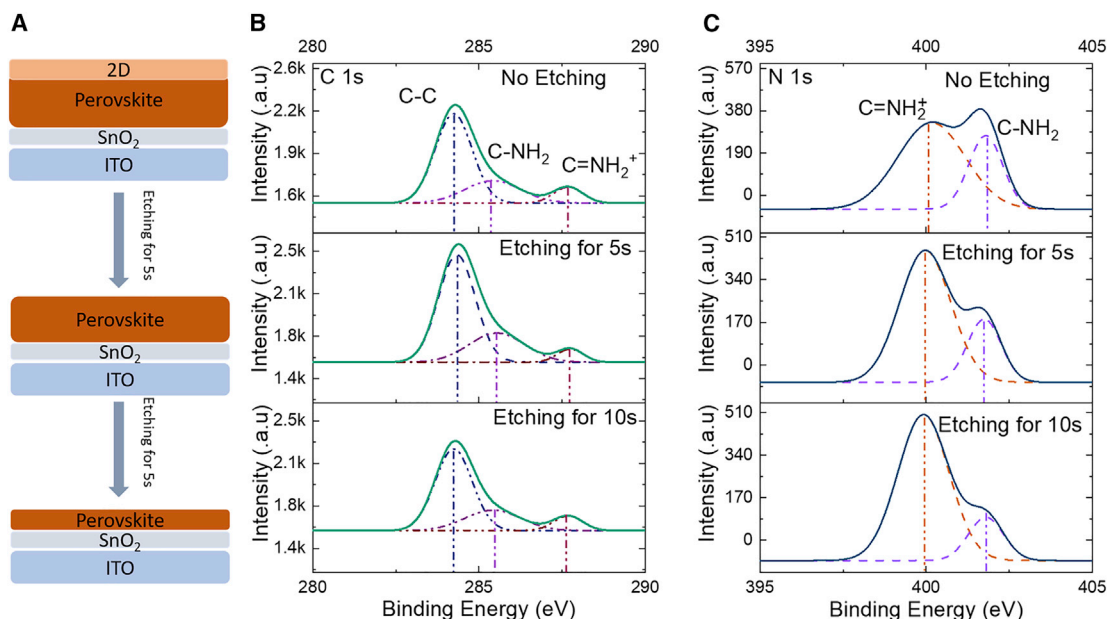


Figure 4. Depth resolved analysis of KI+HABr passivated perovskite thin film

(A) Illustration of depth profiling.

(B) C 1 s spectra for the KI+HABr sample before and after 5 s and 10 s of etching, respectively.

(C) N 1 s spectra for the KI+HABr sample before and after 5 s and 10 s of etching, respectively.

AFM-IR images of the selected regions of the same samples under a higher magnification. The $1,715\text{ cm}^{-1}$ wavenumber was chosen for the AFM-IR mapping due to its prominence in all of the samples (Figure S4), which corresponds to the FA functional group.^{44,45} In Figures 3J–3L, red signifies high FA content, while blue signifies low FA content. After KI incorporation, it can be seen that the FA is significantly depleted at the grain boundaries (Figure 3K), suggesting a redistribution of FA, with FA content being more even distributed within the grain interior and FA being more depleted at the grain boundaries. This is also seen in Figure S5B, which shows a line scan of a KI-incorporated sample. Further HABr treatment does not induce the re-distribution of FA but rather homogenizes the surface by its coverage (Figure 3L).³⁶ This is seen in the results of depth-resolved XPS measurements of the KI+HABr passivated film as shown in Figure 4.

Figure 4A illustrates the XPS measurements carried out on test structures before and after 5 and 10 s of etching. Measurement results are shown in Figure 4B for the C 1 s peaks at 285.4 and 287.7 eV and in Figure 4C for the N 1 s peaks, at 399.8 and 401.2 eV, corresponding to $\text{C}=\text{NH}_2^+$ and $\text{C}-\text{NH}_2$,⁴⁶ which are signatures of 3D and 2D perovskites, respectively.⁴⁶ Identical intensities of C–C peaks in the depth-resolved C 1 s spectra (Figure 4B) suggests negligible surface contamination by air exposure before sample loading for the XPS test. From Figure 4C it can be seen that the surface of the HABr-treated sample is dominated by the $\text{C}-\text{NH}_2$ 2D perovskites, while the bulk is dominated by the $\text{C}=\text{NH}_2^+$ 3D perovskites.

To evaluate the electrical properties of PSCs before and after KI and HABr passivations, Mott-Schottky analysis, temperature-dependent V_{OC} measurement, and impedance spectroscopy were carried out on reference, KI passivated, and KI+HABr passivated PSCs.

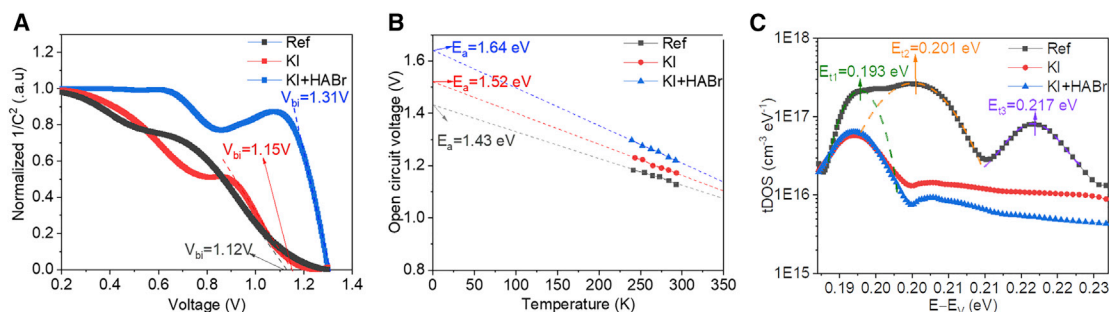


Figure 5. Electrical characterization of KI and HABr PSCs by gas quenching

(A) Mott-Schottky plot.

(B) Temperature-dependent V_{OC} .

(C) Density of trap states as a function of energy level for PSCs before and after passivations.

Figure 5A shows the Mott-Schottky plots for reference, KI passivated, and KI+HABr passivated PSCs for determining their built-in potentials (V_{bi}). Reference and KI passivated cells have similar V_{bi} s at 1.12 and 1.15 V, respectively. The KI+HABr passivated cell has a much higher V_{bi} at 1.31 V. The higher V_{bi} is due to a better band alignment due to the formation of 2D perovskite.³⁶ This explains the higher V_{OC} measured for KI+HABr passivated cells (Figure S1A).

Figure 5B shows the results of the temperature-dependent V_{OC} measurement, which enables the extrapolation of the recombination activation energy (E_a).⁴⁷ E_a was calculated to be 1.43 eV for the reference cell, 1.52 eV for the KI passivated cell, and 1.64 eV for the KI+HABr passivated cell. E_a for the reference cell is lower than its band gap ($E_g = 1.57$ eV from PL spectra), which means the recombination is predominantly at the perovskite surface (i.e., the perovskite-HTM interface).⁴⁷ E_a s for the KI passivated and KI+HABr passivated cell are greater than or equal to their band gaps ($E_{g, KI} = 1.56$ eV and $E_{g, KI+HABr} = 1.56$ eV from their PL spectra). This means carrier recombination via interface, surface, or tail states in these cells has been greatly reduced.⁴⁷

Impedance spectroscopy of the cells also allows for the determination of the density of trap states at different energy levels (E_t) with respect to the valance band (E_v),⁴⁸ as shown in Figure 5C. For the reference, KI passivated and KI+HABr passivated cells E_{t1} , E_{t2} , and E_{t3} were identified and assigned to 0.193 eV, 0.201 eV, and 0.217 eV, respectively. It is clear that KI incorporation effectively passivates the E_{t2} and E_{t3} traps and reduces E_{t1} to a certain extent. HABr surface treatment reduces the density of E_{t2} and E_{t3} traps further, but the density of shallow E_{t1} traps remains unchanged. The E_{t1} traps may be associated with the perovskite-SnO₂ interface or the perovskite bulk. For the latter, trap reduction may be due to the passivation of halide vacancies by the KI.^{34,35} However, E_{t1} traps are insensitive to the HABr surface treatment. The E_{t2} and E_{t3} traps are likely to be associated with the perovskite surface (i.e., perovskite-HTM interface) and therefore were greatly reduced after the HABr treatment, forming a 2D perovskite surface passivation layer that also facilitates better band alignment, enhancing cells' built-in potential to produce higher output voltage.

Preliminary stability testing shows that unprotected cells initially improved during the first 500 h of N₂ storage and retained 91% of the initial PCE after 1 month of storage (Figure S6A; Table S1). After 10 h of thermal stress at 85°C, the efficiency of non-encapsulated cells was halved but recovered (to 97% of initial value) after the removal and redeposition of the hole transport material (HTM) (spiro-OMeTAD)

and the Au electrode (Figure S6B). This indicates that thermal degradation is dominated by the degradation in the spiro-OMeTAD. After 12 h of humidity (50% relative humidity) exposure, the efficiency of non-encapsulated cells dropped by 34% and recovered to only 91% of the initial value after the removal and redeposition of the HTM (spiro-OMeTAD) and the Au electrode (Figure S6C). This suggests that humidity exposure also affects the perovskite absorber. Future work will include optimization for cell stability rather than just performance, which has been the focus of this work.

In summary, we have developed complementary bulk and surface passivation strategies for gas-quenching processed PSCs that involves the incorporation of KI in the perovskite precursor for bulk passivation and a surface treatment using HABr for surface passivation. Spatially resolved analysis reveals that KI induces spatial-compositional change, which helps explain film quality and device improvements. We have also improved the understanding of trap distributions in triple cation perovskites and how the use of KI and HABr reduces traps at different levels. Spatially resolved and depth-resolved chemical analysis reveals that HABr treatment forms a thin 2D perovskite layer on top of the perovskite bulk. Mott-Schottky analysis reveals that HABr greatly improves the built-in potential of the device, thereby improving its output voltage. The best PSC fabricated using KI incorporation and HABr surface treatment achieved a steady-state PCE of 23.6%, with a remarkable V_{oc} of 1.23 V, the highest for perovskite solar cells fabricated by gas quenching to date. The complementary passivations strategies reported here are not only suitable for PSCs fabricated by the gas-quenching method but are also readily translatable to other scalable processes for improving efficiency.

EXPERIMENTAL PROCEDURES

Resource availability

Lead contact

Further information and requests should be directed to and will be fulfilled by the lead contact, Anita W.Y. Ho-Baillie (anita.ho-baillie@sydney.edu.au).

Materials availability

This study did not generate new unique materials.

Data and code availability

The published article includes all of the data analyzed and necessary to reach the conclusions of this study in the figures and tables of the main text and [Supplemental information](#). Further information and requests for additional data should be directed to the lead contact.

Materials and methods

See the [Supplemental experimental procedures](#) for full details of materials, precursor preparation, PSC fabrication, and device characterization.

SUPPLEMENTAL INFORMATION

Supplemental information can be found online at <https://doi.org/10.1016/j.xcrp.2021.100511>.

ACKNOWLEDGMENTS

S.T. is supported by the John Hooke Chair of Nanoscience Postgraduate Research Scholarship and the CSIRO postgraduate research top-up scholarship. T.W.J.,

T.C.-J.Y., and G.J.W. wish to thank the CSIRO Research Office and the Energy Technologies Program for project funding, postgraduate scholarships, and Fellowship support. K.K.-Z. is supported by the Australian Research Council (ARC) Laureate Fellowship grant (FL180100053) and the ARC Centre of Excellence FLEET (CE170100039). Other funding sources include the Australian Renewable Energy Agency (ARENA) through the Australian Centre for Advanced Photovoltaics (ACAP), 2020/RND001 and 2020/RND003. The authors acknowledge the facilities as well as the scientific and technical assistance of the Research & Prototype Foundry Core Research Facility at the University of Sydney, part of the Australian National Fabrication Facility.

AUTHORS CONTRIBUTIONS

Conceptualization, A.W.Y.H.-B.; methodology, A.W.Y.H.-B., and S.T.; investigation, S.T., J.B., J.Z., J.T., Y.L., M.M., Y.C., T.W.J., T.C.-J.Y., L.Y., M.T., H.T.N., M.P.N., and N.J.E.-D.; writing – original draft, S.T.; writing – review & editing, K.K.-Z., G.J.W., S.H., and A.W.Y.H.-B.; funding acquisition, A.W.Y.H.-B.; supervision, S.H., D.R.M., and A.W.Y.H.-B.

DECLARATION OF INTERESTS

A.W.Y.H.-B. is a board member at CRPS. The other authors declare no competing interests.

Received: March 31, 2021

Revised: June 18, 2021

Accepted: June 28, 2021

Published: July 21, 2021

REFERENCES

- Xing, G., Mathews, N., Sun, S., Lim, S.S., Lam, Y.M., Grätzel, M., Mhaisalkar, S., and Sum, T.C. (2013). Long-Range Balanced Electron- and Hole-Transport Lengths in Organic-Inorganic $\text{CH}_3\text{NH}_3\text{PbI}_3$. *Science* 342, 344–347.
- Yin, W.-J., Shi, T., and Yan, Y. (2014). Unusual defect physics in $\text{CH}_3\text{NH}_3\text{PbI}_3$ perovskite solar cell absorber. *Appl. Phys. Lett.* 104, 063903.
- Stranks, S.D., Eperon, G.E., Grancini, G., Menelaou, C., Alcocer, M.J.P., Leijtens, T., Herz, L.M., Petrozza, A., and Snaith, H.J. (2013). Electron-hole diffusion lengths exceeding 1 micrometer in an organometal trihalide perovskite absorber. *Science* 342, 341–344.
- Green, M.A., Ho-Baillie, A., and Snaith, H.J. (2014). The emergence of perovskite solar cells. *Nat. Photonics* 8, 506–514.
- Green, M.A., and Ho-Baillie, A.W.Y. (2019). Pushing to the Limit: Radiative Efficiencies of Recent Mainstream and Emerging Solar Cells. *ACS Energy Lett.* 4, 1639–1644.
- Pham, H.D., Yang, T.C.-J., Jain, S.M., Wilson, G.J., and Sonar, P. (2020). Development of Dopant-Free Organic Hole Transporting Materials for Perovskite Solar Cells. *Adv. Energy Mater.* 10, 1903326.
- Lin, L., Jones, T.W., Yang, T.C.-J., Duffy, N.W., Li, J., Zhao, L., Chi, B., Wang, X., and Wilson, G.J. (2021). Inorganic Electron Transport Materials in Perovskite Solar Cells. *Adv. Funct. Mater.* 31, 2008300.
- National Renewable Energy Laboratory. Best Research-Cell Efficiency Chart. <https://www.nrel.gov/pv/cell-efficiency.html>.
- Jeon, N.J., Noh, J.H., Kim, Y.C., Yang, W.S., Ryu, S., and Seok, S.I. (2014). Solvent engineering for high-performance inorganic-organic hybrid perovskite solar cells. *Nat. Mater.* 13, 897–903.
- Kim, G., Min, H., Lee, K.S., Lee, D.Y., Yoon, S.M., and Seok, S.I. (2020). Impact of strain relaxation on performance of α -formamidinium lead iodide perovskite solar cells. *Science* 370, 108–112.
- Kim, J., Park, B.W., Baek, J., Yun, J.S., Kwon, H.-W., Seidel, J., Min, H., Coelho, S., Lim, S., Huang, S., et al. (2020). Unveiling the Relationship between the Perovskite Precursor Solution and the Resulting Device Performance. *J. Am. Chem. Soc.* 142, 6251–6260.
- Yin, M., Xie, F., Chen, H., Yang, X., Ye, F., Bi, E., Wu, Y., Cai, M., and Han, L. (2016). Annealing-free perovskite films by instant crystallization for efficient solar cells. *J. Mater. Chem. A Mater. Energy Sustain.* 4, 8548–8553.
- Xu, W., Gao, Y., Ming, W., He, F., Li, J., Zhu, X.-H., Kang, F., Li, J., and Wei, G. (2020). Suppressing Defects-Induced Nonradiative Recombination for Efficient Perovskite Solar Cells through Green Antisolvent Engineering. *Adv. Mater.* 32, e2003965.
- Chang, N.L., Ho-Baillie, A.W.Y., Basore, P.A., Young, T.L., Evans, R., and Egan, R.J. (2017). A manufacturing cost estimation method with uncertainty analysis and its application to perovskite on glass photovoltaic modules. *Prog. Photovolt. Res. Appl.* 25, 390–405.
- Zhang, M., Wilkinson, B., Liao, Y., Zheng, J., Lau, C.F.J., Kim, J., Bing, J., Green, M.A., Huang, S., and Ho-Baillie, A.W.-Y. (2018). Electrode Design to Overcome Substrate Transparency Limitations for Highly Efficient 1 cm² Mesoscopic Perovskite Solar Cells. *Joule* 2, 2694–2705.
- Zhang, M., Yun, J.S., Ma, Q., Zheng, J., Lau, C.F.J., Deng, X., Kim, J., Kim, D., Seidel, J., Green, M.A., et al. (2017). High-Efficiency Rubidium-Incorporated Perovskite Solar Cells by Gas Quenching. *ACS Energy Lett.* 2, 438–444.
- Zhang, M., Bing, J., Cho, Y., Li, Y., Zheng, J., Lau, C.F.J., Green, M.A., Huang, S., and Ho-Baillie, A.W.Y. (2019). Synergistic effect of potassium and iodine from potassium triiodide complex additive on gas-quenched perovskite solar cells. *Nano Energy* 63, 103853.
- Conings, B., Babayigit, A., Klug, M.T., Bai, S., Gauquelin, N., Sakai, N., Wang, J.T.-W., Verbeeck, J., Boyen, H.-G., and Snaith, H.J. (2016). A Universal Deposition Protocol for Planar Heterojunction Solar Cells with High Efficiency Based on Hybrid Lead Halide

- Perovskite Families. *Adv. Mater.* **28**, 10701–10709.
19. Babayigit, A., D'Haen, J., Boyen, H.-G., and Conings, B. (2018). Gas Quenching for Perovskite Thin Film Deposition. *Joule* **2**, 1205–1209.
 20. Brinkmann, K.O., He, J., Schubert, F., Malerczyk, J., Kreusel, C., van Gen Hassend, F., Weber, S., Song, J., Qu, J., and Riedl, T. (2019). Extremely Robust Gas-Quenching Deposition of Halide Perovskites on Top of Hydrophobic Hole Transport Materials for Inverted (p-i-n) Solar Cells by Targeting the Precursor Wetting Issue. *ACS Appl. Mater. Interfaces* **11**, 40172–40179.
 21. Lau, C.F.J., Zhang, M., Deng, X., Zheng, J., Bing, J., Ma, Q., Kim, J., Hu, L., Green, M.A., Huang, S., and Ho-Baillie, A. (2017). Strontium-Doped Low-Temperature-Processed CsPbI₂Br Perovskite Solar Cells. *ACS Energy Lett.* **2**, 2319–2325.
 22. Yi, H., Wang, D., Mahmud, M.A., Haque, F., Upama, M.B., Xu, C., Duan, L., and Uddin, A. (2018). Bilayer SnO₂ as Electron Transport Layer for Highly Efficient Perovskite Solar Cells. *ACS Appl. Energy Mater.* **1**, 6027–6039.
 23. Liu, K., Liang, Q., Qin, M., Shen, D., Yin, H., Ren, Z., Zhang, Y., Zhang, H., Fong, P.W.K., Wu, Z., et al. (2020). Zwitterionic-Surfactant-Assisted Room-Temperature Coating of Efficient Perovskite Solar Cells. *Joule* **4**, 2404–2425.
 24. Werner, J., Moot, T., Gossett, T.A., Gould, I.E., Palmstrom, A.F., Wolf, E.J., Boyd, C.C., van Hest, M.F.A.M., Luther, J.M., Berry, J.J., and McGehee, M.D. (2020). Improving Low-Bandgap Tin-Lead Perovskite Solar Cells via Contact Engineering and Gas Quench Processing. *ACS Energy Lett.* **5**, 1215–1223.
 25. Yi, H., Wang, D., Duan, L., Haque, F., Xu, C., Zhang, Y., Conibeer, G., and Uddin, A. (2019). Solution-processed WO₃ and water-free PEDOT:PSS composite for hole transport layer in conventional perovskite solar cell. *Electrochim. Acta* **319**, 349–358.
 26. Yi, H., Duan, L., Haque, F., Bing, J., Zheng, J., Yang, Y., Mo, A.C.-h., Zhang, Y., Xu, C., Conibeer, G., and Uddin, A. (2020). Thiocyanate assisted nucleation for high performance mix-cation perovskite solar cells with improved stability. *J. Power Sources* **466**, 228320.
 27. Lee, D., Jung, Y.-S., Heo, Y.-J., Lee, S., Hwang, K., Jeon, Y.-J., Kim, J.-E., Park, J., Jung, G.Y., and Kim, D.-Y. (2018). Slot-Die Coated Perovskite Films Using Mixed Lead Precursors for Highly Reproducible and Large-Area Solar Cells. *ACS Appl. Mater. Interfaces* **10**, 16133–16139.
 28. Subbiah, A.S., Isikgor, F.H., Howells, C.T., De Bastiani, M., Liu, J., Aydin, E., Furlan, F., Allen, T.G., Xu, F., Zhumagali, S., et al. (2020). High-Performance Perovskite Single-Junction and Textured Perovskite/Silicon Tandem Solar Cells via Slot-Die-Coating. *ACS Energy Lett.* **5**, 3034–3040.
 29. Kim, J.-E., Jung, Y.-S., Heo, Y.-J., Hwang, K., Qin, T., Kim, D.-Y., and Vak, D. (2018). Slot die coated planar perovskite solar cells via blowing and heating assisted one step deposition. *Sol. Energy Mater. Sol. Cells* **179**, 80–86.
 30. Dai, X., Deng, Y., Van Brackle, C.H., Chen, S., Rudd, P.N., Xiao, X., Lin, Y., Chen, B., and Huang, J. (2020). Scalable Fabrication of Efficient Perovskite Solar Modules on Flexible Glass Substrates. *Adv. Energy Mater.* **10**, 1903108.
 31. Deng, Y., Van Brackle, C.H., Dai, X., Zhao, J., Chen, B., and Huang, J. (2019). Tailoring solvent coordination for high-speed, room-temperature blading of perovskite photovoltaic films. *Sci. Adv.* **5**, eaax7537.
 32. Deng, Y., Ni, Z., Palmstrom, A.F., Zhao, J., Xu, S., Van Brackle, C.H., Xiao, X., Zhu, K., and Huang, J. (2020). Reduced Self-Doping of Perovskites Induced by Short Annealing for Efficient Solar Modules. *Joule* **4**, 1949–1960.
 33. Hwang, K., Jung, Y.-S., Heo, Y.-J., Scholes, F.H., Watkins, S.E., Subbiah, J., Jones, D.J., Kim, D.-Y., and Vak, D. (2015). Toward large scale roll-to-roll production of fully printed perovskite solar cells. *Adv. Mater.* **27**, 1241–1247.
 34. Abdi-Jalebi, M., Andaji-Garmaroudi, Z., Cacovich, S., Stavrakas, C., Philippe, B., Richter, J.M., Alsari, M., Booker, E.P., Hutter, E.M., Pearson, A.J., et al. (2018). Maximizing and stabilizing luminescence from halide perovskites with potassium passivation. *Nature* **555**, 497–501.
 35. Zheng, F., Chen, W., Bu, T., Ghiggino, K.P., Huang, F., Cheng, Y., Tapping, P., Kee, T.W., Jia, B., and Wen, X. (2019). Triggering the Passivation Effect of Potassium Doping in Mixed-Cation Mixed-Halide Perovskite by Light Illumination. *Adv. Energy Mater.* **9**, 1901016.
 36. Yoo, J.J., Wieghold, S., Sponseller, M.C., Chua, M.R., Bertram, S.N., Hartono, N.T.P., Tresback, J.S., Hansen, E.C., Correa-Baena, J.-P., Bulović, V., et al. (2019). An interface stabilized perovskite solar cell with high stabilized efficiency and low voltage loss. *Energy Environ. Sci.* **12**, 2192–2199.
 37. Huang, F., Dkhissi, Y., Huang, W., Xiao, M., Benesperi, I., Rubanov, S., Zhu, Y., Lin, X., Jiang, L., Zhou, Y., et al. (2014). Gas-assisted preparation of lead iodide perovskite films consisting of a monolayer of single crystalline grains for high efficiency planar solar cells. *Nano Energy* **10**, 10–18.
 38. Yao, D., Zhang, C., Pham, N.D., Zhang, Y., Tiong, V.T., Du, A., Shen, Q., Wilson, G.J., and Wang, H. (2018). Hindered Formation of Photoinactive δ -FAPbI₃ Phase and Hysteresis-Free Mixed-Cation Planar Heterojunction Perovskite Solar Cells with Enhanced Efficiency via Potassium Incorporation. *J. Phys. Chem. Lett.* **9**, 2113–2120.
 39. Liang, J., Chen, C., Hu, X., Chen, Z., Zheng, X., Li, J., Wang, H., Ye, F., Xiao, M., Lu, Z., et al. (2020). Suppressing the Phase Segregation with Potassium for Highly Efficient and Photostable Inverted Wide-Band Gap Halide Perovskite Solar Cells. *ACS Appl. Mater. Interfaces* **12**, 48458–48466.
 40. Tebyetekerwa, M., Zhang, J., Liang, K., Duong, T., Neupane, G.P., Zhang, L., Liu, B., Truong, T.N., Basnet, R., Qiao, X., et al. (2019). Quantifying Quasi-Fermi Level Splitting and Mapping its Heterogeneity in Atomically Thin Transition Metal Dichalcogenides. *Adv. Mater.* **31**, e1900522.
 41. Peng, B., Mei, H., Zhang, H., Shao, H., Xu, K., Ni, G., Jin, Q., Soukoulis, C.M., and Zhu, H. (2019). High thermoelectric efficiency in monolayer PbI₂ from 300 K to 900 K. *Inorg. Chem. Front.* **6**, 920–928.
 42. Xu, J., Buin, A., Ip, A.H., Li, W., Voznyy, O., Comin, R., Yuan, M., Jeon, S., Ning, Z., McDowell, J.J., et al. (2015). Perovskite-fullerene hybrid materials suppress hysteresis in planar diodes. *Nat. Commun.* **6**, 7081.
 43. Cho, D., Hwang, T., Cho, D.-g., Park, B., and Hong, S. (2018). Photoconductive noise microscopy revealing quantitative effect of localized electronic traps on the perovskite-based solar cell performance. *Nano Energy* **43**, 29–36.
 44. Szostak, R., Silva, J.C., Turren-Cruz, S.-H., Soares, M.M., Freitas, R.O., Hagfeldt, A., Tolentino, H.C.N., and Nogueira, A.F. (2019). Nanoscale mapping of chemical composition in organic-inorganic hybrid perovskite films. *Sci. Adv.* **5**, eaaw6619.
 45. Tennyson, E.M., Abdi-Jalebi, M., Ji, K., Garrett, J.L., Gong, C., Pawlicki, A.A., Ovchinnikova, O.S., Munday, J.N., Stranks, S.D., and Leite, M.S. (2020). Correlated Electrical and Chemical Nanoscale Properties in Potassium-Passivated, Triple-Cation Perovskite Solar Cells. *Adv. Mater. Interfaces* **7**, 2000515.
 46. Zhou, Q., Liang, L., Hu, J., Cao, B., Yang, L., Wu, T., Li, X., Zhang, B., and Gao, P. (2019). High-Performance Perovskite Solar Cells with Enhanced Environmental Stability Based on a (p-FC6H4C2H4NH3)2[PbI4] Capping Layer. *Adv. Energy Mater.* **9**, 1802595.
 47. Tress, W., Yavari, M., Domanski, K., Yadav, P., Niesen, B., Correa Baena, J.P., Hagfeldt, A., and Graetzel, M. (2018). Interpretation and evolution of open-circuit voltage, recombination, ideality factor and subgap defect states during reversible light-soaking and irreversible degradation of perovskite solar cells. *Energy Environ. Sci.* **11**, 151–165.
 48. Duan, H.-S., Zhou, H., Chen, Q., Sun, P., Luo, S., Song, T.-B., Bob, B., and Yang, Y. (2015). The identification and characterization of defect states in hybrid organic-inorganic perovskite photovoltaics. *Phys. Chem. Chem. Phys.* **17**, 112–116.